J. Water Environ. Nanotechnol., 8(1): 79-93 Winter 2023

ORIGINAL RESEARCH PAPER

Fabrication of $MnWO_4$ modified ZnS nanocomposite as an effective nanoadsorbent: Experimental investigation and neural network modeling

Balasubramani Kavitha [1,*], Selvam Sharumathi [1], Subburam Sivakumar [2,*]

[1] P.G and Research Department of Chemistry, C.P.A. College, Bodinayakanur, Tamilnadu, India.
[2] Department of Computer Science, C.P.A. College, Bodinayakanur, Tamilnadu, India.

Received: 2022-09-20 Accepted: 2022-12-20 Published: 2023-02-12

ABSTRACT

The purpose of this study was to determine the adsorptive characteristics of a $MnWO_4$/ZnS nanocomposite for removing Amaranth dye from an aqueous solution. A simple chemical precipitation approach was used to make the $MnWO_4$/ZnS nanocomposite. The crystal structure, morphology, and pore size of the resulting nanocomposites were evaluated by UV-vis-DRS, FT-IR, XRD, SEM, and EDAX. In a laboratory batch adsorption experiment, the effect of operational parameters such as adsorbent dose, starting dye concentration, agitation speed, contact time, and temperature was investigated to optimize the conditions for maximum amaranth removal. To reduce the number of trials and the associated costs, an artificial neural network (ANN) was used to forecast dye removal effectiveness. With a tangent sigmoid transfer function (tansig) at the hidden layer and a linear transfer function (purelin) at the output layer, a backpropagation neural network with Levenberg–Marquardt training algorithm was utilized to predict adsorption efficiency. For amaranth dye, a contact time of 180 minutes, an adsorbent dosage of 0.35 g/L, and an initial dye concentration of 10 µM resulted in a 96 % dye removal. Different models were used to fit the equilibrium isotherm data. Langmuir and Temkin models have high R^2 and are in good agreement with the experimental data (0.9966 and 0.9927). The pseudo-second-order model is appropriate to describe the experimental data, and film diffusion may be involved in the sorption process, according to the kinetic analysis. When the experimental data was compared to the dye adsorption efficiency predicted by the artificial neural network model, it was discovered that this model can accurately predict the behavior of the amaranth dye adsorption process on $MnWO_4$/ZnS under various conditions.

Keywords: MnWO4/ZnS, Artificial neural network, Amaranth dye

How to cite this article
Kavitha B., Sharumathi S., Sivakumar S., Fabrication of $MnWO_4$ modified ZnS nanocomposite as an effective nanoadsorbent: Experimental investigation and neural network modeling. J. Water Environ. Nanotechnol., 2023; 8(1): 79-93 DOI: 10.22090/jwent.2023.08.008

INTRODUCTION

The usage of dyestuff has risen worldwide as a result of rising industrialization and other human activities [1]. As a result of the rise of various industries such as paper, cosmetics, and textiles, water pollutants such as dyes have generated a critical environmental concern in recent years [2-4]. Toxic colors affect not just surface water sources but also groundwater in trace amounts as a result of soil leaching after rain and snow [5]. Because of their toxicity, accumulation, and magnification throughout the food chain, increasing quantities of these pollutants in the ecosystem pose a serious health risk. To reduce the negative effects of dyes, numerous methods for removing large amounts of dyes from aqueous solutions have been used. Different ways of eliminating colors and organic pollutants from wastewater include chemical precipitation [6] membrane separation [7] (coagulation-flocculation [8] biological [9], electrochemical treatments [10], and catalytic

* Corresponding Authors Email: *sivaku2002@yahoo.com*
kaviravee@gmail.com

This work is licensed under the Creative Commons Attribution 4.0 International License.
To view a copy of this license, visit http://creativecommons.org/licenses/by/4.0/.

reduction [11]. Because of its low starting cost, flexibility in design, ease of operation, and intensity to biological materials in an aqueous environment, adsorption has shown to be a handy and successful approach [12].

The adsorption process is one of the most efficient methods for the removal of dyes due to its high efficiency, ease of operation, and cost-effectiveness, which has been considered by many researchers. [13-18] A wide range of adsorbents (activated carbon, zeolites, clays, industrial by-products, agricultural wastes, biomass, and polymeric materials) have been investigated for dye-loaded wastewater remediation; however, the majority of these adsorbents suffer from low uptake capacity and separation/recovery inconvenient [19]. The development of novel low-cost adsorbents with a high surface area and a rich chemical activity may now be possible because of the development of nanotechnology, leading to better techniques for water remediation. The functional components for the adsorption of both organic and inorganic molecules are called nano sorbents. Nanoadsorbents are highly effective at removing contaminants through adsorption, offer great potential for cleaning up pollutants in wastewater and air and provide new opportunities for environmental applications. The ongoing search for novel adsorbents that can rapidly and effectively remove colors from water, synthetic, and real industrial effluents is a consequence [20, 21].

Because of their enormous surface area, availability of active sites on the surface of such adsorbents, and great stability and regeneration capacities, the development of nanoscale materials as adsorbents has brought tremendous improvements in adsorption technology. Several remarkable composite nanomaterials made with metal oxides, metal tungstates, and organic polymers, among others, have been reported in recent research for extremely successful dye-contaminated water remediation [22-24. Due to their unusual physical and chemical features, such as their usage as semiconducting, optical, magnetic, and catalytic materials [24, 26], transition metal chalcogenides have gotten a lot of attention in the last decade. Cadmium sulfide [27], zinc sulfide [28], silver sulfide [29], and several distinct phases of copper sulfides [30] (are all important transition metal sulfides. Zinc sulfide (ZnS), a broadband gap II–VI compound semiconductor, is a promising material for diverse applications in photovoltaics, electroluminescence devices, bioimaging technologies, light emitting devices, catalysis and sensors, solar energy cells, and other fields [31 - 34]. $MnWO_4$ is a semiconductor with a low band gap (2.8 eV) that has piqued researchers‘ interest due to its unusual multiferroic, electrochemical, and ionic properties, as well as potential applicability in gas sensors, catalysts, and electrochromic devices [35]. In recent years, the potential of single zinc sulfides and manganese tungstates for adsorptive color removal from aqueous solution has been investigated. To our knowledge, the adsorption of dyes on a nanocomposite containing a mixed phase of ZnS (zinc blende) and $MnWO_4$ (monoclinic) has not been investigated.

The adsorption was investigated using a one-variable-at-a-time method, with the effective factors being contact time, pH, adsorbent dosage, agitation speed, pollutant concentration, and temperature. The issue is that during a multivariate performance, the approach changes one of the parameters while keeping the other terms constant. As a result, it has negative impacts on adsorption, which should be investigated using multivariate approaches [36, 37]. Adsorption as a process is made up of input variables like effective variables and output responses like efficiency. The efficiency value is affected by the number of effective variables that change. Therefore, the amount of the variable could be optimized to achieve the maximum efficiency that is free of the mentioned complexities [38, 39]. A possible alternative modeling technique is artificial neural networks (ANN). Modeling based on artificial neural networks has the advantage of not requiring a mathematical description of the phenomena involved in the process, which could be useful in simulating and scaling up complex photodegradation systems. The choice of process, as well as the accessible collection of data and domain for training purposes, all influence the success of building a trustworthy and robust network.

The synthesis of $MnWO_4$/ZnS nanocomposite as an inorganic adsorbent was reported in this paper using a simple and low-cost approach. UV-Vis-DRS, FT-IR, XRD, SEM, and EDAX techniques were used to characterize the resulting adsorbent. The adsorbent was made and utilized as an adsorbent to remove amaranth dye from an aqueous solution. Artificial neural networks were used to analyze and optimize the effects of key parameters (starting dye concentration, adsorbent dosage, contact time, agitation speed, and temperature). The resulting results were compared to the experimental results.

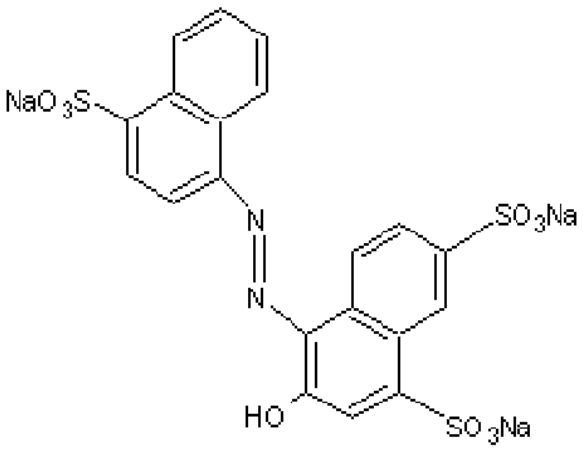

Fig. 1. Chemical structure of Amaranth Dye

EXPERIMENTAL

Chemicals

The chemical structure of amaranth or Food Red 9 or Acid Red 27 with chemical formula $C_{20}H_{11}N_2Na_3O_{10}S_3$ are shown in Fig. 1. The maximum absorption was observed at a wavelength of 523 nm. All chemicals including amaranth, $MnCl_2$, NH_4WO_4, $(CH_3COO)_2Zn$, Na_2S, and C_2H_5OH with the highest purity available were purchased from Merck, India.

Preparation of Manganese tungstate

A simple co-precipitation approach is used to make $MnWO_4$ nanoparticles. As a starting material, manganese chloride ($MnCl_2$) was employed. $MnCl_2$ was typically dissolved in 100 mL of distilled water. While NH_4WO_4 was dissolved in 50ml distilled water and the solution was added until complete precipitation, the resulting solution was continuously stirred. The precipitate was filtered and rinsed carefully with distilled water until it was free of Cl^- ions after another 3 hours of stirring. Finally, the precipitate was dried for 2 hrs at 120°C before being calcined for 5 hrs at 500°C [40].

Preparation of zinc sulfide

Chemical methods were used to make ZnS nanoparticles. For the synthesis of ZnS nanoparticles, sodium sulfide ($Na_2S.7H_2O$) and zinc acetate ($(CH_3COO)_2Zn$) were utilized as reactants. 1 M solution of each component was made in distilled water using the stoichiometric ratio in grams. For the synthesis of nanoparticles at room temperature, freshly prepared aqueous solutions of these compounds were employed. Under continuous stirring, the sodium sulfide solution was added drop by drop to the zinc acetate solution until white precipitates appeared. To finish the reaction, stirring was done for 20 minutes, then the precipitate was agitated for another 3 hours. The precipitate was dried for 1 hour at 100 °C and then calcined for 2 hours at 250°C [41].

Preparation of $MnWO_4$/ZnS

Co-precipitation was used to make $MnWO_4$/ZnS nanoparticles. 5 g of $MnWO_4$ and 3.075 g of ZnS were dissolved in 60 ml of ethanol. Both are combined and sonicated for 30 minutes, followed by 3 hours of continuous stirring. Finally, the resulting suspension was filtered, washed, and dried at 100 °C for 1 hour before being calcined at 500°C for 2 hours.

Characterization

The following procedures were used to characterize the nanoparticles. Using a JASCO V-550 double-beam spectrophotometer with a PMT detector equipped with an integrating sphere assembly and $BaSO_4$ as a reference sample, diffuse reflectance spectra for dry-pressed disc samples were obtained. The spectra were taken at room temperature and ranged from 200 to 800 nanometers. JASCO-4200 FT-IR spectrometer was used to record the FT-IR spectra of the prepared catalyst. X-ray powder diffraction with Cu k radiation at 25°C was used to determine the structure and phase of the samples, and structural assignments were established using the standard

Table 1: Range of variables

S.No	Variables	Ranges
	Input Variables	
1	Amount of adsorbent dose (g/L)	0.1 – 0.5
2	Initial concentration of Amaranth	10 - 50
3	Contact time (min)	15 – 100
4	Agitation speed (rpm)	100 – 800
	Output variables	
5	Amaranth removal efficiency (%)	0 - 100

JCPDS powder diffraction data. The average crystallite size was determined by applying the Debye-Scherrer formula [42]:

$$D=0.9\lambda/\beta Cos\theta \quad (1)$$

Where λ is the X-ray wavelength, θ is the Bragg diffraction angle, and β is the FWHM of the XRD peak appearing at the diffraction angle θ.

A JM 6701F-6701 scanning electron microscope (SEM) was used to image the nanoparticles in both secondary and backscattered electron modes. The elemental analysis was detected by energy-dispersive X-ray spectroscopy (EDX) attached to the SEM.

Adsorption studies

The 0.35 g/L of $MnWO_4$/ZnS was mixed with 300 mL dye solution at pH 7 as a single solution in a Round Bottom Flask (RB flask) and the mixture was stirred by a magnetic stirrer with a constant speed of 300 rpm for 30 min until equilibrium. The adsorbent was separated from the solution by centrifugation at 3500 rpm for 5 min and subsequently, the adsorption of the Amaranth solution was recorded by UV-vis spectrophotometer JASCO V-550 at 523 nm. Finally, their concentration was calculated based on a calibration curve obtained at the same conditions. The equilibrium adsorption capacity, (q_e(mg/g)) was calculated using the following equation:

$$q_e=(C_0-C_e)\ V/W \quad (2)$$

$$\%\ Removal = C_0 - C_e/C_0 * 100$$

Where,C_0 and C_e(mg/L) were initial and equilibrium dyes concentrations, respectively;

W and V are the mass of the adsorbent (g) and the solution volume (L).

Definition of the ANN model

The prediction of amaranth dye adsorption efficiency from an aqueous environment utilizing $MnWO_4$/ZnS is a difficult task, hence a neural network approach is used. The researchers utilized a three-layer ANN with a tangent sigmoid transfer function (tansig) in the hidden layer and a linear transfer function (purelin) in the output layer. The designed networks were trained using Levenberg–Marquardt backpropagation (trainlm) with 1000 iterations. In the hidden layer, the number of neurons was tuned between 1 and 10. Using the MATLAB R20011a program, the data collected from the experimental values for the adsorption efficiency of amaranth dye were used to train a network model that could compute the anticipated adsorption efficiency values from the inputs. The ANN model was created using forty experimental sets. All experimental data for amaranth dye adsorption efficiency were separated into three groups at random (70 % for training and 15 % for testing and 15 %; for validation). The starting amaranth concentration, adsorbent dosage, contact time, and Agitation speed were used as input factors, with adsorption efficiency being the output parameter. Table1 summarises the range of variables that were used. The entire data set was normalized in the 0–1 range. As a result, data (X_i) is converted to a normalized value (X_{normal}) in the following manner [38, 39] :

$$X_{normal} = \frac{X_i - X_{min}}{X_{max} - X_{min}} \quad (3)$$

$_{min}$ and X_{max} are the minimum and maximum actual experimental data. The input signals are modified by interconnection weight known as a weight factor (W_{ij}), which represents the interconnection of i^{th} node of the first layer to j^{th} node of the second layer. The sum of modified

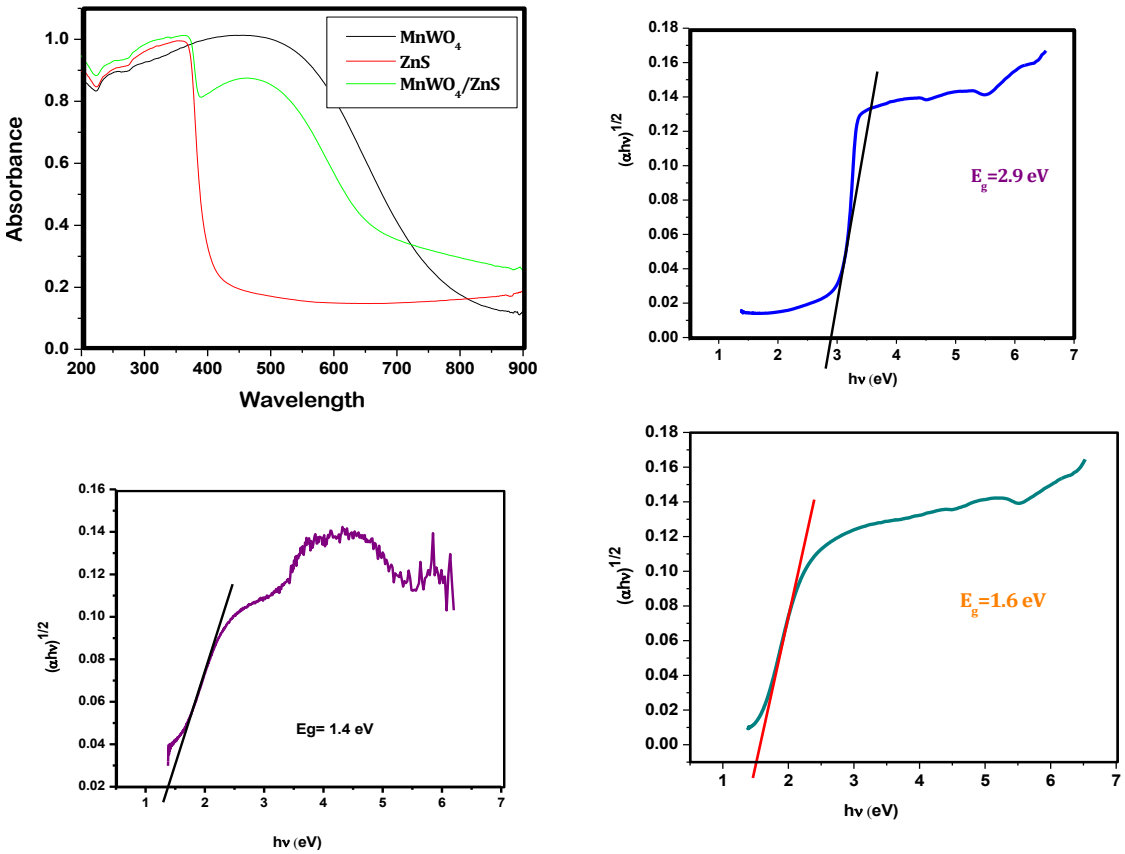

Fig. 2. (a) UV-Vis -DRS spectra of $MnWO_4$, ZnS, and $MnWO_4$/ZnS. (b) Tauc plot of $MnWO_4$, (c) Tauc plot of ZnS, (d) Tauc plot of $MnWO_4$/ZnS

signals (total activation) is then modified by a sigmoid transfer function and output is collected at the output layer.

The results of the various networks structure and training procedures were compared based on the mean squared error (MSE) and the coefficient of determination (R^2) which can be defined as follows [43]:

$$MSE = \frac{1}{N}\sum_{i=1}^{N}\left(\left|y_{prd,i} - y_{exp.i}\right|\right)^3 \quad (4)$$

RESULT AND DISCUSSION

UV-DRS

The UV-Vis diffuse reflectance spectra of $MnWO_4$, ZnS, and $MnWO_4$/ZnS are shown in Fig. 2. (a).In comparison with ZnS and $MnWO_4$ the absorption edge of $MnWO_4$/ZnS is slightly shifted toward the visible region. The observed redshift is ascribed to the element interaction of ZnS and $MnWO_4$.The optical band gaps for the $MnWO_4$, ZnS, and $MnWO_4$/ZnS are calculated based on the optical spectral absorption using the following well-known relation [44, 45]:

$$(\alpha h\upsilon)^2 = C\left(h\upsilon - E_g\right) \quad (5)$$

where hν is photon energy and C is a constant, and α is the absorption coefficient. Fig. 2. (b),(c) and (d) show the plot of $(\alpha h\upsilon)^{1/2}$ vs. (hυ) for the $MnWO_4$, ZnS, and $MnWO_4$/ZnS nanoparticles. The band gap values obtained by extrapolating the straight line portion to the energy axis at zero absorption coefficients give the direct optical band gaps of $MnWO_4$, ZnS, and $MnWO_4$/ZnS as 2.9eV, 1.4eV, and 1.6eV, respectively.

X-Ray Diffraction (XRD)

The XRD pattern of $MnWO_4$, ZnS, and $MnWO_4$/ZnS nanoparticles is shown in Fig. 3. XRD analyses were performed to determine the crystalline structure and phase formation of $MnWO_4$, ZnS, and $MnWO_4$/ZnS nanoparticles. The pattern of ZnS displays the Zinc blend structure(JCPDS No 5-0566).Three diffraction peaks at 2θ values of 28.96, 48, and 56.52. The peaks were identified to

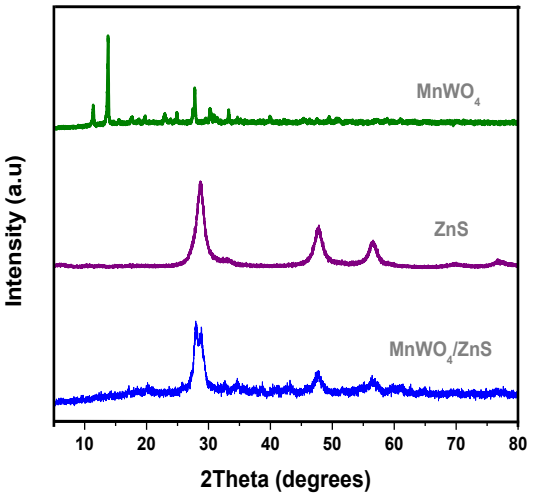

Fig. 3. XRD spectra of $MnWO_4$, ZnS, and $MnWO_4$/ZnS

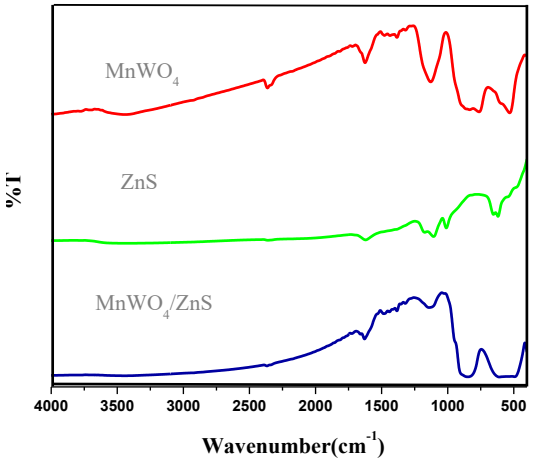

Fig. 4. FT-IR spectra of $MnWO_4$, ZnS and $MnWO_4$/ZnS

originate from (111), (220), and (311) planes of the cubic zinc-blende phase of ZnS, respectively. The $MnWO_4$ is nearly located JCPDS NO: 800135 and the peaks are identified as monoclinic structures. The diffraction peaks of $MnWO_4$ can ascribe to structure. The major peaks for the doped ZnS appeared to be slightly reduced. Therefore, it can be concluded that $MnWO_4$ does not change the crystalline phase and the crystallinity of ZnS [46].

The average crystalline sizes $MnWO_4$, ZnS, and $MnWO_4$/ZnS are calculated as 39, 40, and 36 nm respectively. The crystalline sizes of the Nanocomposites are lower than the $MnWO_4$ and ZnS favored good adsorptive activity.

FT-IR spectral analysis

The FT-IR spectra of pure $MnWO_4$, ZnS, and $MnWO_4$/ZnS are exhibited in Fig. 4, They are recorded within the range of 4000 cm^{-1} – 400 cm^{-1}. $MnWO_4$ shows a characteristic stretching absorption band in the region 2000 – 400 cm^{-1}. The band saw at 875 and 861 cm^{-1} in the FTIR spectra of $MnWO_4$ and $MnWO_4$/ZnS is attributed to stretching vibrations of the Mn-O bond and at 531 cm^{-1} is symmetrical vibrations of the Mn-W-O groups. Moreover, the strong band located at 604 cm^{-1} is attributed to the asymmetrical stretching vibrations of the W–O bond in the $(W_2O_4)_n$ chain. Broadband near 3200 cm^{-1} corresponds to the stretching vibration of O-H of the adsorbed water molecule. The peaks appearing at 490, 615, and 1110 cm^{-1} belong to ZnS vibration. The presence of peaks between 1150 – 1800 cm^{-1} may be due to the sulfur-oxygen interaction and the adsorption of water molecules on the surface of nanoparticles [47, 48].

SEM and EDAX

The SEM image of $MnWO_4$, ZnS, and $MnWO_4$/ZnS nanocomposites were analyzed by SEM and are displayed in Fig. 5 (a), (b), and (c) respectively. From Fig. 5 (a) the nanosized $MnWO_4$ particles show nanorod structure. From Fig. 5 (b) the nanosized ZnS particles show nanosphere structure. Fig. 5 (c) shows the SEM image of a $MnWO_4$/ZnS nanorod with a sphere-like structure. From Fig. 5 (c), it was observed that the average crystalline size was found to be 35 - 45 nm which is in good agreement with the XRD results. The corresponding EDAX spectrum and result of $MnWO_4$/ZnS are displayed in Fig. 5 (d). It can be seen that the $MnWO_4$/ZnS consist of Mn, W, Zn, O, and S. The corresponding keV values are given in Table 2.

Adsorption activity

Effect of contact time of Amaranth Dye

One of the most critical parameters for a cost-effective wastewater treatment system is contact time. The adsorption of Amaranth onto $MnWO_4$/ZnS was investigated over a contact time range of 0-180 minutes to establish the required adsorption equilibrium period. At various times, the batch equilibrium adsorption time of $MnWO_4$/ZnS was examined (0, 30, 60, 90, 120, 150, and 180). As shown in Fig. 6 the rapid uptake of the dye and the establishment of equilibrium within a short period indicated the efficiency of the adsorbent for its use

Table 2: Energy value of elements

S.No	Element	keV
1	O	1.20
2	S	0.28
3	Zn	0.36
4	Mn	0.79
5	W	0.49

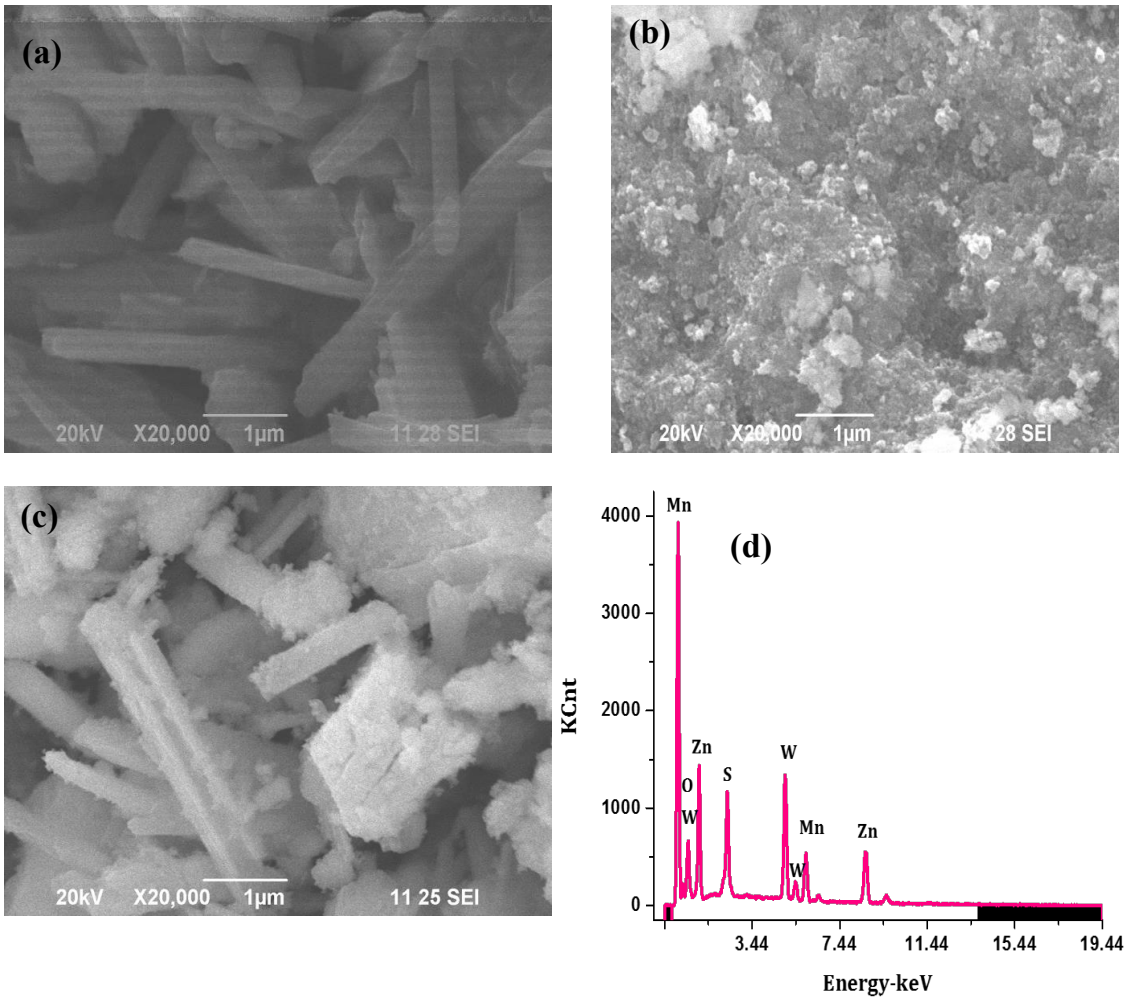

Fig. 5 (a)SEM image of $MnWO_4$, (b)SEM image of ZnS, (c) SEM image of $MnWO_4$/ZnS, (d) EDAX spectrum of $MnWO_4$/ZnS

in wastewater treatment. It can be seen that the removal of the dye reaches the maximum at 90 min. This indicates that the rate of adsorption is very fast; and after that, no significant change in the extent of adsorption was observed. The final equilibrium time significantly depends on the initial dye concentrations and amount of adsorbent. The adsorption efficiency increases with rising contact time [49].

Effect of adsorbent dosage on the removal of Amaranth

In this method, several experiments were carried out with varied amounts of adsorbent ranging from 0.1 to 0.5 g/L, Amaranth concentration of 10 µM, and agitation rate of 300 rpm, respectively. Fig. 6 (b) shows the proportion of Amaranth removed as a function of adsorbent mass. Beyond 0.35 g/L, the reduction in the quantity of dye adsorbed

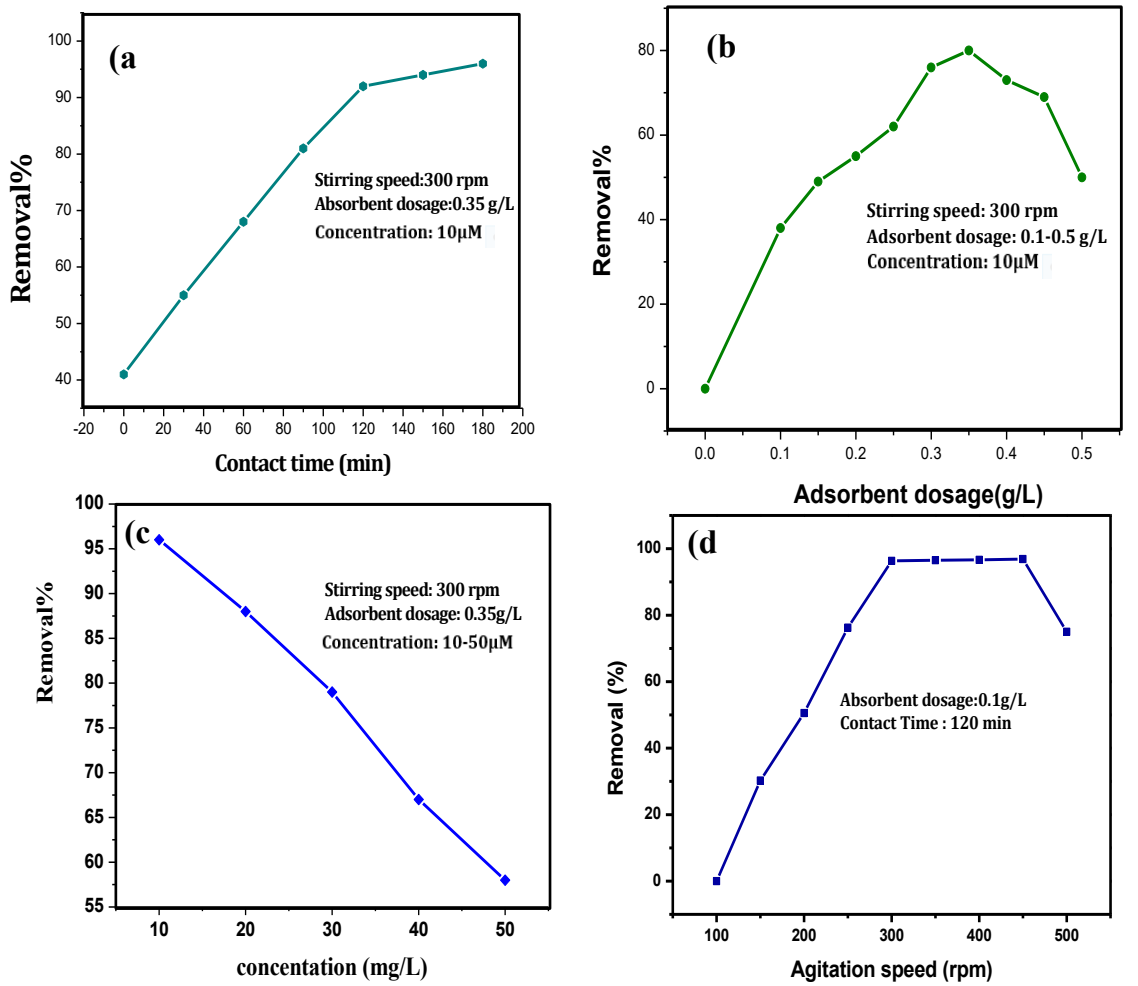

Fig. 6 (a). Effect of contact time (min), (b) Effect of adsorbent dosage, 7 (c).Effect of Dye concentration, 7 (d). Effect of agitation speed

onto the unit weight of the adsorbent is attributed to the overlapping or aggregation of adsorption sites, which leads to a decrease in total available adsorbent surface area and an increase in diffusion path length. It was found that by raising the adsorbent mass at all conditions, the maximum removal percentage was achieved at a lower required contact time [50, 51].

Effect of Dye concentration

The effect of Amaranth concentrations ranging from 10 to 50 µM on its adsorption by $MnWO_4$/ZnS was investigated, and the percentage of Amaranth removal at various concentrations is depicted in Fig. 6. (c). As shown, the actual amount of Amaranth absorption increased as dye concentrations increased, however, the removal percentage decreased as dye concentrations increased, owing to saturation and occupation of accessible sites on the adsorbents. This effect is connected to the decrease in the mass gradient between the solution and adsorbents. At dye concentrations, the solute-to-adsorbent unoccupied sites ratio is large and produces an increase in color removal [52].

Effect of agitation speed

Fig. 6 (d) shows the effect of agitation speed (100, 200, and 300 rpm) on the dye adsorption at dye concentrations of 10µM. It is clear that while increasing the mixing rate from 100 to 300 rpm, the adsorption capacity varied at a dye concentration of 10 µM. This could be due to the fact that increasing the mixing rate facilitates keeping the particles in a suspension and deagglomeration state, thereby increasing the contact surface solid-liquid and

Table 3: Different kinetic model parameters

Models	Parameters	$MnWO_4$/ZnS
	$q_{e,\ exp}$ (mg/g)	9.6589
Pseudo-first order model	R^2	0.7482
	k_1 (min^{-1})	1.7288
	$q_{e,\ cal}$(mg/g)	0.120
Pseudo-second order model	R^2	0.999
	k_2 (g/mg min)	0.7664
	q_{tcal}(mg/g)	9.6711

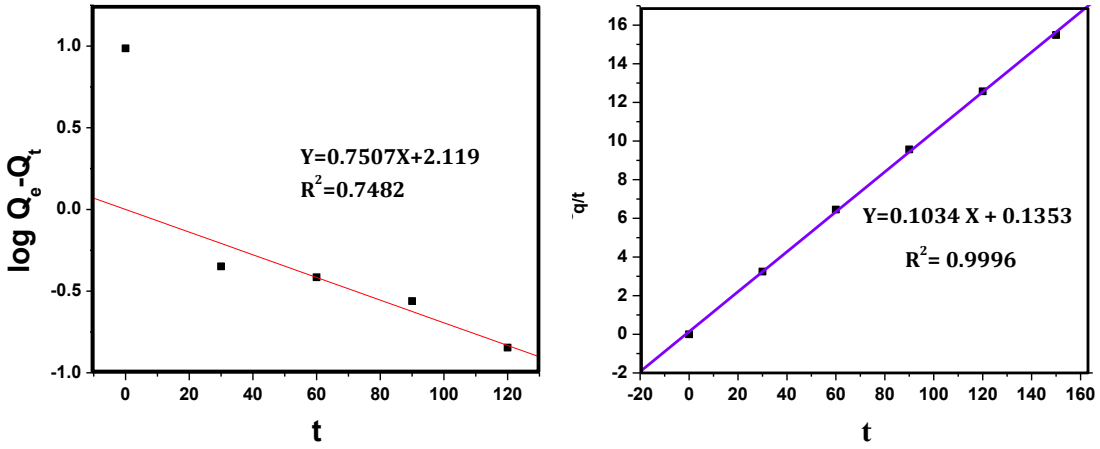

Fig. 7 (a) Pseudo-first-order kinetics for adsorption of Amaranth onto $MnWO_4$/ZnS. (b) Pseudo-second-order kinetics for adsorption of Amaranth onto $MnWO_4$/ZnS

favoring the transfer of the dye molecules to the adsorption sites [53, 54].

Adsorption kinetics

The kinetics of Amaranth adsorption on $MnWO_4$/ZnS must be known in order to choose the best operating conditions. Pseudo-first-order and pseudo-second-order kinetics were used to investigate Amaranth adsorption onto $MnWO_4$/ZnS. The correlation coefficients and deviation of experimental and calculated adsorption capacity were used to express the conformity between experimental data and the well-known equation of the above-mentioned model. The equations for the pseudo-first-order and pseudo-second-order adsorption models are as follows [55, 56] :

Pseudo-first-order equation: $\log (q_e\text{-}q_t) = \log (q_e) - (K_1/2.303)\ t$ (6)

Pseudo-second-order equation: $t/q_t = (1/K_2 q_e^{\ 2}) + (1/q_e)\ t$ (7)

Where q_e and q_t are the amounts of Amaranth adsorbed on the adsorbent (mg g^{-1}) at equilibrium and at time t (min); K_1 is the pseudo-first-order adsorption constant (min^{-1}) and K_2 is the pseudo-second-order adsorption rate constant (g(mg min^{-1}). Both models were tested for applicability over a period ranging from 0 to 120 minutes (10, 20, 30, 40, and 50 µM). The kinetic parameters were calculated using correlation coefficients (R) and the adsorption capacity was calculated. It was discovered that the pseudo-second-order equation best describes the adsorption of Amaranth, implying that the rate-limiting step may be the adsorption mechanism rather than mass transport. Fig. 7 (a) and (b) show the plot of pseudo-first-order and pseudo-second-order kinetics and the calculated values are listed in the Table 2.

Adsorption isotherm

Adsorption isotherm studies are useful in establishing the relationship between the quantity of dye adsorption and the equilibrium concentration of adsorbate in the reaction mixture in order to successfully employ the adsorption technique for practical reasons. Thus, the isotherm models Langmuir, Freundlich, and Tempkin are used for the experimental data collected during the isotherm adsorption experiments (Table 3).

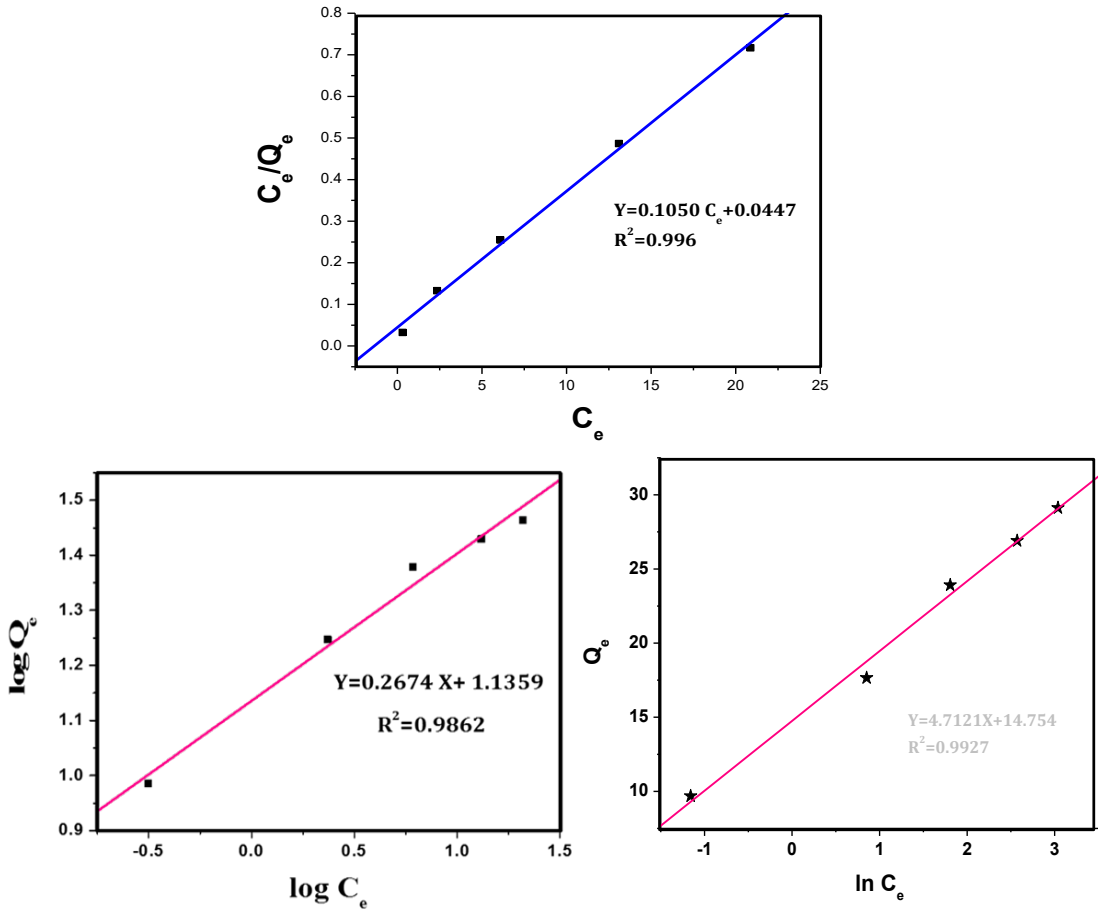

Fig. 8. Langmuir isotherm for adsorption of amaranth onto $MnWO_4$/ZnS, (b) Freundlich isotherm adsorption of amaranth onto $MnWO_4$/ZnS, (c) Tempkin isotherm adsorption of Amaranth onto $MnWO_4$/ZnS

Langmuir adsorption isotherm

The Langmuir equation [57, 58] is given by

$$q_e = q_{max} K_L C_e / 1 + K_L C_e \quad (8)$$

where q_{max} is the maximum adsorption capacity corresponding to complete monolayer coverage on the surface (mg/g) and K_L is the Langmuir constant (L/mg).

The above equation can be written in a linear form;

$$\mathbf{C_e / q_e = 1 / q_{max} K_L + C_e / q_{max}} \quad \mathbf{(9)}$$

The constants can be evaluated from the intercepts and the slopes of the linear plots of C_e/q_e versus C_e (Fig. 8 (a)).

Freundlich adsorption isotherm

The Freundlich equation describes heterogeneous systems. It can be characterized by the heterogeneity factor 1/n. The equation can be defined as [59, 60] (Tao et al., 2014):

$$q_e = K_F C_e^{1/n} \quad (10)$$

Where K_F is the Freundlich constant (mg/g) (L/mg)$^{1/n}$ and 1/n is the heterogeneity factor. A linear form of the Frundlich model can be written by taking the logarithms of the equation;

$$\ln q_e = \ln K_F + 1/n \ln C_e \quad (11)$$

The constant K_F and exponent 1/n can be obtained from the intercepts and the slopes of the linear plots of $\ln q_e$ versus $\ln C_e$ (Fig. 8 (b).

Temkin adsorption isotherm

The Temkin isotherm can be simplified to the following equation;

$$Q_e = B_1 \ln K_T + B_1 \ln C_e \quad (12)$$

Where $B_1 = (RT)/b$ is related to the heat of adsorption, T is the absolute temperature in Kelvin and R is the universal gas constant, 8.314 (J mol^{-1} K^{-1}) (Fig. 8 (c).

Mechanism of the dye adsorption process

The interactions between the dye molecules

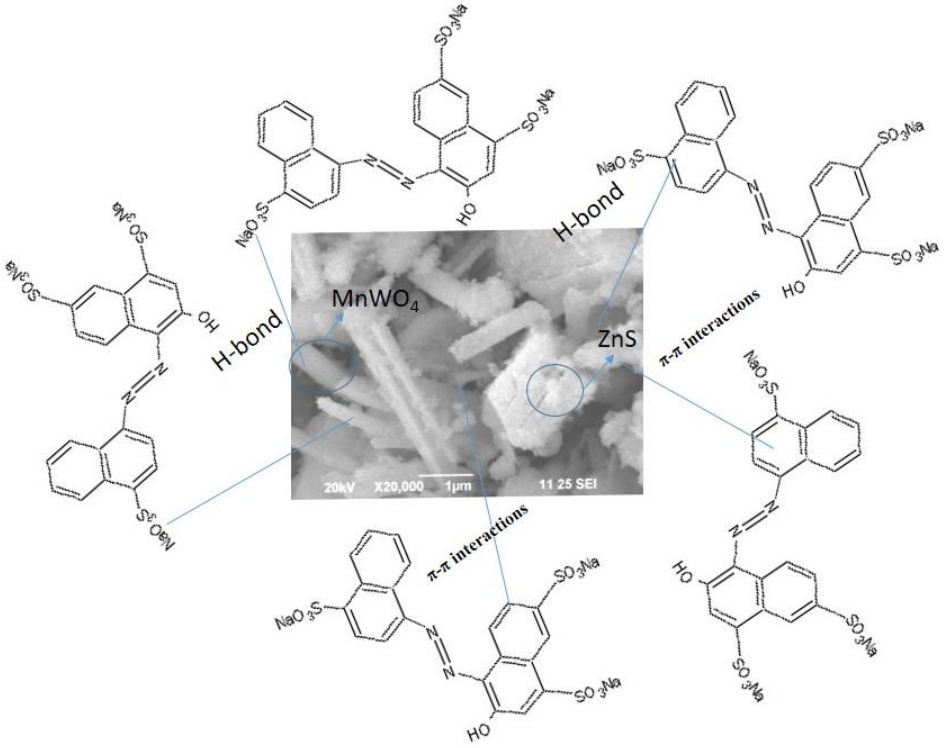

Fig. 9 Schematic diagram for proposed adsorption mechanism of Amaranth dye on $MnWO_4$/ZnO

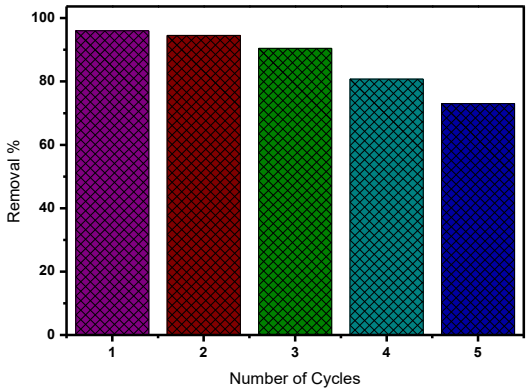

Fig. 10 Regeneration of MnWO4/ZnO after removal of Amaranth dye

and the adsorbent, which mostly involve hydrogen bonds, electrostatic bonding interactions, and π-π interactions, are what drive the dye adsorption process [61]. Fig. 9 schematizes the anticipated interactions between the $MnWO_4$/ZnO NPs and the Amaranth dye. The π-π interactions are present between the π bonds of the aromatic ring present in the dye molecule and Zn, Mn atom which contains vacant d-orbitals. Additionally, Zn and Mn can provide electrons to the Amaranth dye molecule's vacant π* orbitals. This adsorption method's synergic effect is the development of this particular type of bond between Mn, Zn, and dye molecules within the system. There are more adsorbent molecules and sites for adsorption due to the complex structure of amaranth dye, which can keep the metal atom in its cavity-like region and reduce the agglomeration of $MnWO_4$/ZnO NPs [62, 63].

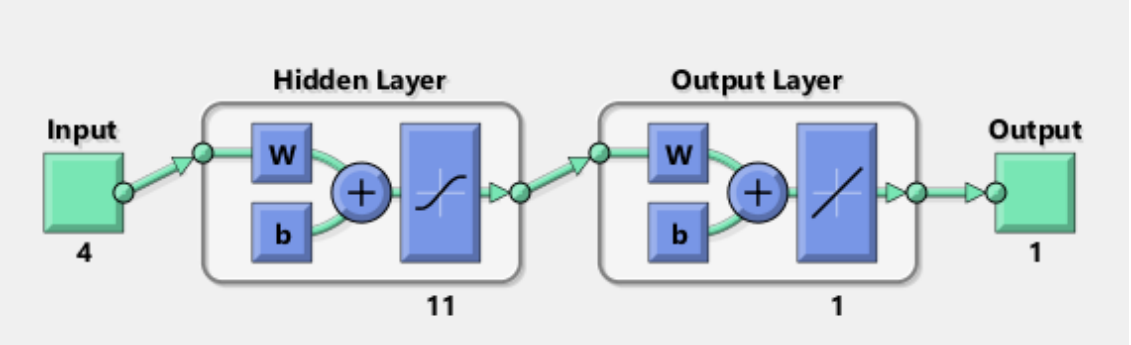

Fig.11 Proposed ANN structure

The polarised nitrogen and oxygen atoms in the dye molecule and the oxygen atoms in $MnWO_4$/ZnO form hydrogen bonds in addition to the interaction. Additionally, the SO_3Na group in the Amaranth dye molecule forms an H-bond with the $MnWO_4$/ZnO oxygen atom [64]. As a result, interactions between the adsorbent and adsorbate as well as the surface area of the adsorbent, the heterogeneous and non-uniform sites accessible for adsorption, and the charge produced on the surface all play a role in the adsorption of Amaranth dye by $MnWO_4$/ZnO NPs.

Regeneration and reusability

The regeneration study was carried out with 10 µM Amaranth solution and 0.35 g/L adsorbent dosage. The adsorbents were desorbed by a 0.1 mol/L NaOH solution for 180 min after adsorbing amaranth for 180 min, and they were subsequently activated by a 0.1 mol/L HCl solution. Results were displayed in Fig. 10 by cycle. The first three cycles' removal efficiencies, which are 96 %, 94 %, and 90 %, respectively, are still quite high. The removal efficiency starts to decline after the fourth cycle and peaks at 72% after the sixth. This might be due to the fact that when the number of cycles rises, the majority of the adsorption active sites become occupied. As a result, there aren't any vacant adsorption sites accessible, which directly affects removal efficiency.

Optimization of neural networks

During the network design process, designing an appropriate neural network is a critical task. Not all algorithms and transfer functions may work for all processes. The training process, transfer function, and the number of neurons in each layer are all highly important characteristics to consider when designing a network. If the model fails to match the experimental data, the output value from the water treatment plant will be erratic, making it impossible to govern. To discover the best network model, the trial and error method was used. It has been discovered that 10 neurons generate the lowest mean square error value (MSE) [64, 65]. The proposed optimal ANN structure is shown in Fig. 11. There are three layers to the ANN: input, hidden, and output. Four neurons in the input layer employ a tangent sigmoid activation function. The hidden layer contains 11 neurons with tangent sigmoid activation functions, and the output layer contains one neuron with a linear activation function.

In the beginning, one neuron in the hidden layer was picked. The MSE value was shown to decrease as the number of neurons increased. The MSE values for 2 (MSE= 0.48086) and 4 (MSE=0.6143) neurons in the hidden layer were significantly higher. The MSE value drops from 0.4727 to 0.0878 as the number of hidden neurons increases from 5 to 8. The MSE value decreased as the number of hidden neurons increased, reaching a minimal value (MSE=0.00975) at 11 hidden neurons. As a result, the neural network with 11 hidden neurons was chosen as the best scenario. When the number of neurons in the hidden layer was increased to 12, the MSE value was increased to 0.0173. The MSE value increased dramatically as the number of neurons in the hidden layer increased (Fig. 10) The network response between ANN outputs and the relevant targets was analyzed using regression analysis. Fig. 12 shows the graphical output of the network outputs shown against the targets as open circles and R^2 is almost 0.99414. The computed and experimental results agree the best, demonstrating that the BP – ANN is a potent fitting and forecasting tool for describing adsorption behavior.

CONCLUSION

In this work, $MnWO_4$/ZnS has been synthesized and effectively utilized as an Adsorbent for the

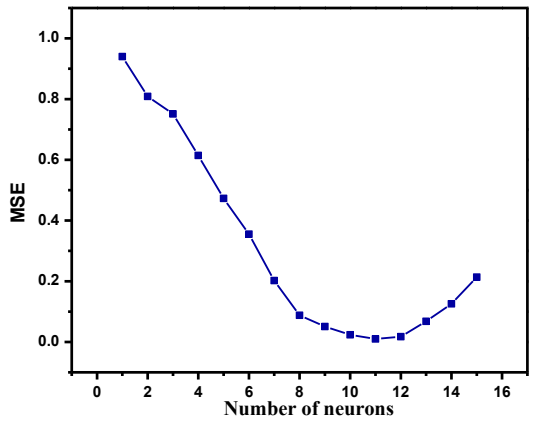

Fig. 12 Regression analysis for adsorption of amaranth onto $MnWO_4$/ZnS

removal of Amaranth. The prepared nanoparticles have been characterized using UV-Vis - DRS, FT-IR, XRD, SEM, and EDAX techniques. $MnWO_4$/ZnS shows higher adsorbent activity (96%). The result of this research work may be used for the remediation of organic dyes in the environment. The adsorption of $MnWO_4$/ZnS was investigated using different variables, amount of adsorbent, concentrations, contact time, agitation speed, the adsorption isotherm, and adsorption kinetics. Equilibrium isotherm data were fitted using different models. Among them, models, Langmuir model, and Temkin model are in good agreement with the experimental data with high R. Kinetic study showed that the pseudo-second-order model is appropriate to describe the experimental and film diffusion that might be involved in the sorption process. The adsorption process was optimized using ANN. The network was trained by using a back propagation LM algorithm with 11 neurons in the hidden layer. Minimum MSE (0.00975) and maximum R^2 (0.9941) was obtained for optimal ANN structure.

CONFLICT OF INTEREST

The authors declare no conflict of interest.

REFERENCES

1. Algadami A.A., Naushad, M., Abdalla, M.A., Khan, M. R., Alothman, Z.A., Adsorptive Removal of Toxic Dye Using Fe3O4-TSC Nanocomposite: Equilibrium, Kinetic, and Thermodynamic Studies, J. Chem. Eng. Data, 2016; 61: 3806-3813 https://doi.org/10.1021/acs.jced.6b00446
2. Grag, A., Sangal, V.K., Bajpai, P.K., Decolorization and degradation of Reactive Black 5 dye by photocatalysis: modeling, optimization and kinetic study, Desalin. Water Treat., 2016; 57: 18003. https://doi.org/10.1080/19443994.2015.1086697
3. Mahmoodi, N.M., Farahani, Z.H., Chamani, H. Dye adsorption from single and binary systems using NiO-MnO2 nanocomposite and artificial neural network modelling, Environ. Prog. Sustain. Energy. 2017, 36(1), 111. https://doi.org/10.1002/ep.12452
4. Mahmoodi, N.M., Manganese ferrite nanoparticle: Synthesis, characterization, and photocatalytic dye degradation ability, Desalin. Water Treat., 2015, 53, 84-90. https://doi.org/10.1080/19443994.2013.834519
5. Yetilmezsoy, K., Demirel, S., Artificial neural network (ANN) approach for modeling of Pb(II) adsorption from aqueous solution by Antep pistachio (Pistacia Vera L.) shells, J. Hazard. Materials, 2008, 152, 1288. https://doi.org/10.1016/j.jhazmat.2007.09.092
6. Zaki, N.G., Khahab, I.A., EI-Monem, N.M.A., Removal of some heavy metals by CKD leachate, J. Hazard. Mat. 2007, 147, 21. https://doi.org/10.1016/j.jhazmat.2006.12.057
7. Zeng, G., Ye, Z., He, Y., Yang, X., Ma, J., Shi, H., Feng, Z., Application of dopamine-modified halloysite nanotubes/PVDF blend membranes for direct dyes removal from wastewater, Chem. Eng. J, 2017, 323, 572. https://doi.org/10.1016/j.cej.2017.04.131
8. Lau, Y.Y., Wong, Y.S., Teng, T.T., Morad, N., Rafatullah, M., Ong, S.A., Coagulation-flocculation of azo dye Acid Orange 7 with green refined laterite soil, Chem. Eng. J. 2014, 246, 383. https://doi.org/10.1016/j.cej.2014.02.100
9. Punzi, M., Anbalagan, A., Borner, R.A., Svensson, B.M., Jonstrup, M., Mattiasson, B., Degradation of a textile azo dye using biological treatment followed by photo-Fenton oxidation: Evaluation of toxicity and microbial community structure, Chem. Eng. J. 2015, 270, 290. https://doi.org/10.1016/j.cej.2015.02.042
10. Bansalah, N., Alfaro, M.Q., Martinez-Huitle, C., Electrochemical treatment of synthetic wastewaters containing Alphazurine A dye, Chem. Eng. J. 2009, 149 348. https://doi.org/10.1016/j.cej.2008.11.031
11. Jin, L., Zhao, X., Ye, J., Qian, X., Dong, M., MOF-derived magnetic Ni-carbon submicrorods for the catalytic reduction of 4-nitrophenol, Catal. Commun, 2017, 107, 43-47. https://doi.org/10.1016/j.catcom.2017.11.014
12. Dai, J., Sun, J., Xie, A., He, J., Li, C., Yan, Y., Designed preparation of 3D hierarchically porous carbon material via solvothermal route and in situ activation for ultrahigh-efficiency dye removal: adsorption isotherm, kinetics and thermodynamics characteristics, RSC Adv. 2016, 6, 3446. https://doi.org/10.1039/C5RA24774H
13. Khan, A., Roy, A., Bhasin, S., Emran, T.B., Khusro, A., Eftekhari, A., Moradi, O., Rokni, H., Karimi, F., Nanomaterials: an alternative source for biodegradation of toxic dyes, Food Chem. Toxicol., 2022. 112996 https://doi.org/10.1016/j.fct.2022.112996
14. Mahmoud, M.E., Amira, M.F., Seleim, S.M., Nabil, G.M., Abouelanwar, M.E., Multifunctionalized graphene oxide@ nanopolyaniline@ zirconium silicate nanocomposite for rapid microwable removal of dyes, J. Nanostructure Chem. 2021, 11, 645. https://doi.org/10.1007/s40097-021-00390-0
15. Mansur, S., Othman, M.H.D., Abidin, M.N.Z., Malek, N.A.N.N., Ismail, A.F., Kadir, S.H.S. A., Goh, P.S., Abdullah, M.S., Asraf, M.H., Dual-layer hollow fibre haemodialysis membrane for effective uremic toxins removal with minimal bloodbacteria contamination, Alex. Eng. J. 2022, 61, 10139.

https://doi.org/10.1016/j.aej.2022.03.043
16. Moneer, A.A., El-Mallah, N.M., El-Sadaawy, M.M., Khedawy, M., Ramadan, M.S., Kinetics, thermodynamics, isotherm modeling for removal of reactive Red 35 disperse yellow 56 dyes using batch bi-polar aluminum electrocoagulation, Alex. Eng. J. 2021, 60, 4139. https://doi.org/10.1016/j.aej.2021.02.061
17. Baloo, L., Isa, M.H., Sapari, N.B., Jagaba, A.H., Wei, L.J., Yavari, S., Razali, R., Vasu, R., Adsorptive removal of methylene blue and acid orange 10 dyes from aqueous solutions using oil palm wastes-derived activated carbons. Alex. Eng. J. 2021, 60, 5611. https://doi.org/10.1016/j.aej.2021.04.044
18. Vo, T.K., Trinh, T.P., Nguyen, V.C., Kim, J., Facile synthesis of graphite oxide/MIL101(Cr) hybrid composites for enhanced adsorption performance towards industrial toxic dyes. J. Ind. Eng. Chem. 2021. 95, 224-234. https://doi.org/10.1016/j.jiec.2020.12.023
19. Faghihi, A., Vakili, M. H., Hosseinzadeh, G., Farhadian, M., Jafari, Z., Synthesis and application of recyclable magnetic freeze-dried graphene oxide nanocomposite as a high capacity adsorbent for cationic dye adsorption, Desalin. Water Treat. 2016, 57, 40502. https://doi.org/10.1080/19443994.2015.1134357
20. Osagie, C., Othmani, A., Ghosh, S., Malloum, A., Esfahani, Z.K., Ahmadi, S., Dyes adsorption from aqueous media through the nanotechnology: A review, J. Mater. Res. Technol. 2021, 14, 2195. https://doi.org/10.1016/j.jmrt.2021.07.085
21. Edson da S. Reis, Filipe D.S. Gorza, Graciela da C. Pedro, Bruna G. Maciel, Romario J. da Silva, Gabriela P. Ratkovski, Celso P. de Melo, (Maghemite/Chitosan/Polypyrrole) nanocomposites for the efficient removal of Cr (VI) from aqueous media, J. Environ. Chem. Eng. 2021; 9: 104893 https://doi.org/10.1016/j.jece.2020.104893
22. Zhao, X., Ma, K., Jiao, T., Xing, R., Ma, X., Hu, J., Huang, H., Zhang, L., Yan, X., Fabrication of Hierarchical Layer-by-Layer Assembled Diamond-based Core-Shell Nanocomposites as Highly Efficient Dye Absorbents for Wastewater Treatment, Sci. Rep. 2017, 7, 44076. https://doi.org/10.1038/srep44076
23. Zhao, X., Zhang, G., Zhang, Z., TiO2-based catalysts for photocatalytic reduction of aqueous oxyanions: State-of-the-art and future prospects, Environ. Int. 2020, 136, 105453. https://doi.org/10.1016/j.envint.2019.105453
24. Xing, R., Wang, W., Jiao, T., Ma, K., Zhang, Q., Homg, W., Qiu, H., Zhou, J., Zhang, L., Peng, Q., BioinspiredPolydopamine Sheathed Nanofibers Containing Carboxylate Graphene Oxide Nanosheet for High-Efficient Dyes Scavenger, ACS Sustainable Chem. Eng. 2017, 5, 4948. https://doi.org/10.1021/acssuschemeng.7b00343
25. Gao, M.R., Xu, Y.F., Jiang, J., Yu, S.H., Nanostructured metal chalcogenides: synthesis, modification, and applications in energy conversion and storage devices, Chem. Soc. Rev. 2013, 42, 2986. https://doi.org/10.1039/c2cs35310e
26. Kershaw, S.V., Susha, A.S., Rogach, A.L., Narrow bandgap colloidal metal chalcogenide quantum dots: synthetic methods, heterostructures, assemblies, electronic and infrared optical properties, Chem. Soc. Rev. 2013, 42, 3033. https://doi.org/10.1039/c2cs35331h
27. Kristl, M., Ban, I., Danc, A., Danc, V., Drofenik, M., A sonochemical method for the preparation of cadmium sulfide and cadmium selenide nanoparticles in aqueous solutions, Ultrason. Sonochem. 2010, 17, 916. https://doi.org/10.1016/j.ultsonch.2009.12.013
28. Behboudnia, M., Majlesara, M.H., Khanbabaee, B., Preparation of ZnSnanorods by ultrasonic waves, Mater. Sci. Eng. B. 2005, 122 160. https://doi.org/10.1016/j.mseb.2005.05.001
29. Kristl, M., Gyergyek, S., Kristl, J., Synthesis and characterization of nanosized silver chalcogenides under ultrasonic irradiation, Mater. Express. 2015, 5, 359. https://doi.org/10.1166/mex.2015.1245
30. Kristl, M., Hojnik, N., Gyergyek, S., Drofenik, M., Synthesis of nickel and cobalt sulfide nanoparticles using a low cost sonochemical method, Mater. Res. Bull. 2013, 48, 1184. https://doi.org/10.1016/j.materresbull.2012.12.020
31. Suo, B., Su, X., Wu, J., Chen, D., Wang, A., Guo, Z., Poly (vinyl alcohol) thin film filled with CdSe-ZnS quantum dots: Fabrication, characterization and optical properties, Mater. Chem. Phys. 2010, 119, 237. https://doi.org/10.1016/j.matchemphys.2009.08.054
32. Maleki, M., Mirdamadi, S., Ghasemzadeh, R., Ghamsari, M. S., Effect of sulfur precursor on dimensions of one-dimensional CdS nanocrystals, J. Mater. Sci. Technol. 2009, 25, 462.
33. John, R., Florence, S.S., Optical, structural and morphological studies of bean- like ZnS nanostructures by aqueous chemical method, Chalcogenide. Lett. 2010, 7, 269.
34. Ponzoni, A., Comini, E., Sbervcglieri, G., Zhou, J., Deng, S.Z., Xu, N.S., Ding, Y., Wang, Z.L., Ultrasensitive and highly selective gas sensors using three-dimensional tungsten oxide nanowire networks, Appl. Phys. Lett. 2006, 88, 203101. https://doi.org/10.1063/1.2203932
35. Khaksar, M., Boghaei, D.M., Amini, M., Synthesis, structural characterization and reactivity of manganese tungstate nanoparticles in the oxidative degradation of methylene blue, Comptes. Rendus. Chimie, 2015, 18, 199. https://doi.org/10.1016/j.crci.2014.04.004
36. Ahmad, Z.K., Yao, L., Lian, Q., Islam, F.,. Zappi, M.E., Gang, D.D., The use of artificial neural network (ANN) for modeling adsorption of sunset yellow onto neodymium modified ordered mesoporous carbon, Chemosphere, 2020, 256, 127081. https://doi.org/10.1016/j.chemosphere.2020.127081
37. Ghaedi, M., Ghaedi, A.M., Abdi, F., Roosta, M., Sahraei, R., Daneshfar, A., Principal component analysis-artificial neural network and genetic algorithm optimization for removal of reactive orange 12 by copper sulfide nanoparticles-activated carbon, J. Ind. Eng. Chem. 2014, 20, 787. https://doi.org/10.1016/j.jiec.2013.06.008
38. Ghaedi, M., Ghaedi, A.M., Hossainpour, M., Ansari, A., Habibi, M.H., Asghari, A.R. Least square-support vector (LS-SVM) method for modeling of methylene blue dye adsorption using copper oxide loaded on activated carbon: Kinetic and isotherm study, J. Ind. Eng. Chem. 2014; 20, 1641. https://doi.org/10.1016/j.jiec.2013.08.011
39. Ghaedi, M., Ansari, A., Assefi Nejad, P., Ghaedi, A., Vafaei, A., Habibi, M.H. Artificial neural network and bees algorithm for removal of Eosin B using cobalt oxide nanoparticle-activated carbon: Isotherm and Kinetics study, Environ. Prog. Sustain. 2015, 34, 155. https://doi.org/10.1002/ep.11981
40. Li, F., Xu, X., Huo, J., Wang, W., A simple synthesis of MnWO4 nanoparticles as a novel energy

storage material, Mater. Chem. Phys. 2015, 167, 22. https://doi.org/10.1016/j.matchemphys.2015.06.029
41. Yesu Thangam Y., Anitha R., Kavitha B., Novel method to synthesize and characterize Zinc Sulfide, Int. J. Appl. Sci. Eng, Res, 2012; 1(2) 282. https://doi.org/10.6088/ijaser.0020101029
42. Zhao, Z., Wang, M.H., Liu, T.T., Tribulus terrestris leaf extract assisted green synthesis and gas sensing properties of Ag-coated ZnO nanoparticles, Mater. Let. 2015, 158, 274-277. https://doi.org/10.1016/j.matlet.2015.05.155
43. Zhang, Y., Dai, M., Liu, K., Peng, C., Du, Y., Chang, Q., Ali, I., Naz, I., and Saroj, D.P., Appraisal of Cu(II) adsorption by graphene oxide and its modelling via artificial neural network, RSC Adv., 2019, 9, 30240. https://doi.org/10.1039/C9RA06079K
44. He, H.Y., Huang, J.F., Cao, L.Y., Wu, J.P., Photodegradation of methyl orange aqueous on MnWO4 powder under different light resources and initial pH, Desalination 2010, 252 , 66. https://doi.org/10.1016/j.desal.2009.10.024
45. Guo, Z., Huo, W., Cao, T., Liu, X., Ren, S., Yang, J., Ding, H., Chen, K., Dong, F., Zhang, Y., Heterojunction interface of zinc oxide and zinc sulfide promoting reactive molecules activation and carrier separation toward efficient photocatalysis, J. Colloid Interface Sci. 2021, 588, 826. https://doi.org/10.1016/j.jcis.2020.11.118
46. You, J., Liu, C., Feng, X., Lu, Xia, L., Zhuang, X., In situ synthesis of ZnS nanoparticles onto cellulose/chitosan sponge for adsorption-photocatalytic removal of Congo red, Carbohydr. Polym., 2022, 288, 119332. https://doi.org/10.1016/j.carbpol.2022.119332
47. Yan, X., Liu, K., Shi, W., Facile synthesis of CdS/MnWO4 heterojunction with enhanced visible-light-driven photocatalytic activity and mechanism investigation, Colloids Surfaces A Physicochem, Eng. Asp. 2017, 520, 138. https://doi.org/10.1016/j.colsurfa.2017.01.065
48. Rema Devi, B. S., Raveendran, R., Vaidyan, A. V., Synthesis and characterization of Mn2+-doped ZnS nanoparticles, Pramana, 2007, 68(4), 679. https://doi.org/10.1007/s12043-007-0068-7
49. Ghasemi, M., Amin, J.A., Effect of pH on Green Synthesis of Reduced Graphene Oxide Using Lemon Extract and Application of Fe3O4/RGO nanocomposites for the removal of Pb (II) from aqueous solution, J. Water Environ. Nanotechnol., 2022; 7(1): 101-120.
50. Shen, X., Gao, X., Wei, W., Zhang, Y., Zhang, Y., Ma, L., Liu, H., Han, R., & Lin, J., Combined performance of hydroxyapatite adsorption and magnetic separation processes for Cd(II) removal from aqueous solution. J. Dispersion Sci. Technol. 2021, 42 (5), 664. https://doi.org/10.1080/01932691.2019.1703734
51. Ravanan, M., Ghaedi, M., Ansari, A., Taghizadeh, F., Elhamifar, D., Comparison of the efficiency of Cu and silver nanoparticle loaded on supports for the removal of Eosin Y from aqueous solution: Kinetic and isotherm study, Spectrochim. Acta. A. Mol. Biomol. Spectrosc. 2014, 123, 467. https://doi.org/10.1016/j.saa.2013.12.049
52. Senguttuvan, S., Janaki, V., Senthilkumar, P., Kannan, S.K., Polypyrrole/zeolite composite - A nanoadsorbent for reactive dyes removal from synthetic solution, Chemosphere, 2022, 287(2), 132164. https://doi.org/10.1016/j.chemosphere.2021.132164
53. Hii, H.T., Adsorption isotherm and kinetic models for removal of methyl orange and remazol brilliant blue R by coconut shell activated carbon, Trop. Aquat. Soil Pollut. 2021, 1(1), 1. https://doi.org/10.53623/tasp.v1i1.4
54. Palai, P., Muduli, S., Priyadarshini, B., Sahoo, T.R., A facile green synthesis of ZnO nanoparticles and its adsorptive removal of Congo red dye from aqueous solution. Mater. Today: Proceedings. 2021, 38, 2445. https://doi.org/10.1016/j.matpr.2020.07.387
55. Janmohammadi, M., Baghdadi, M., Adyel, T.M., Mehrdadi, N., Waste plastic filter modified with polyaniline and polypyrrole nanoparticles for hexavalent chromium removal, Sci. Total Environ. 2021, 752, 141850. https://doi.org/10.1016/j.scitotenv.2020.141850
56. Jasper, E.E., Ajibola, V.O., Onwuka, J.C., Nonlinear regression analysis of the sorption of crystal violet and methylene blue from aqueous solutions onto an agrowaste derived activated carbon, Appl. Water Sci. 2021, 10 (6), 132. https://doi.org/10.1007/s13201-020-01218-y
57. Giri, S. K., Sahoo, P., Das, R., Das, N., Coke/Fe3O4 nanoparticle composites: synthesis, characterization and adsorption behaviour towards organic dyes. Desalin. Water Treat. 2015, 57, 17483. https://doi.org/10.1080/19443994.2015.1085447
58. El Messaoudi, N., El Khomri, M., Fernine, Y., Bouich, A., Lacherai, A., Jada, A., Sher, F., X. Lima, E.C., Hydrothermally engineered Eriobotrya japonica leaves/MgO nanocomposites with potential applications in wastewater treatment, Groundw. Sustain. Dev. 2022, 16, 100728. https://doi.org/10.1016/j.gsd.2022.100728
59. Tao, H., Xuehui, R., Zhijuan, L., Chunge, N , Jide, W., Xintai, S., Synthesis of magnetic separable iron oxide/carbon nanocomposites for efficient adsorptive removal of Congo red. J. Alloy. Comp. 2014, 617, 76. https://doi.org/10.1016/j.jallcom.2014.07.111
60. Jasper, E.E., Ajibola, V.O., Onwuka, J.C., Nonlinear regression analysis of the sorption of crystal violet and methylene blue from aqueous solutions onto an agrowaste derived activated carbon, Appl. Water Sci. 2020, 10 (6), 132. https://doi.org/10.1007/s13201-020-01218-y
61. Al-Degs, Y.S., El-Barghouthi, M.I., El-Sheikh, A.H., Walker, G.M., Effect of solution pH, ionic strength, and temperature on adsorption behavior of reactive dyes on activated carbon, Dyes Pigments, 2008, 77, 16. https://doi.org/10.1016/j.dyepig.2007.03.001
62. Abdulhameed, A.S., Firdaus Hum, N.N.M., Rangabhashiyam, S., Jawad, A.H., Wilson, L. D., Yaseen, Z.M., Al-Kahtani, A.A., ALOthman, Z.A., Statistical modeling and mechanistic pathway for methylene blue dye removal by high surface area and mesoporous grass-based activated carbon using K2CO3 activator, J. Environ. Chem. Eng. 2021; 9 (4): 105530. https://doi.org/10.1016/j.jece.2021.105530
63. Chang, B.P., Gupta, A., Mekonnen, T.H., Flame synthesis of carbon nanoparticles from corn oil as a highly effective cationic dye adsorbent, Chemosphere, 2021, 282, 131062. https://doi.org/10.1016/j.chemosphere.2021.131062
64. Niaei, A., Badiki, T.M., Nabavi, S.R., Salari, D., Izadkhah, B., Caylak, N., Neuro-genetic aided design of modified H-ZSM-5 catalyst for catalytic conversion of methanol to gasoline range hydrocarbons, J Taiwan Inst Chem Eng. 2013, 44(2), 247. https://doi.org/10.1016/j.jtice.2012.11.008
65. Fahadia, M., Nabavia, S.R., Chaichi, M.J., Mesoporous Fe3O4/graphene oxide nanohybrid for catalytic Ozonation: Preparation, characterization and process modeling by neural network, J. Taiwan Inst. Chem. Eng. 134, 2022, 104278. https://doi.org/10.1016/j.jtice.2022.104278